

Rational Design of Covalent Cobaloxime–Covalent Organic Framework Hybrids for Enhanced Photocatalytic Hydrogen Evolution

Kerstin Gottschling, Gökçen Savasci, Hugo Vignolo-González, Sandra Schmidt, Philipp Mauker, Tanmay Banerjee, Petra Rovó, Christian Ochsenfeld, and Bettina V. Lotsch*



Cite This: *J. Am. Chem. Soc.* 2020, 142, 12146–12156



Read Online

ACCESS |



Metrics & More

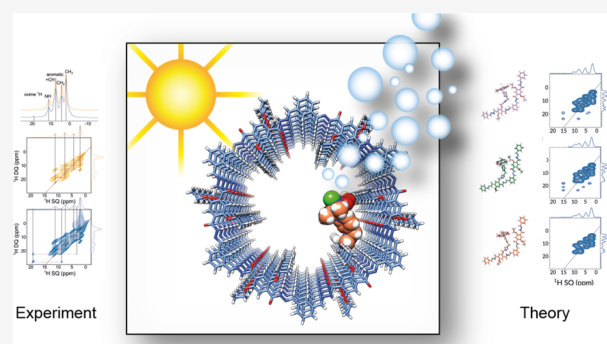


Article Recommendations



Supporting Information

ABSTRACT: Covalent organic frameworks (COFs) display a unique combination of chemical tunability, structural diversity, high porosity, nanoscale regularity, and thermal stability. Recent efforts are directed at using such frameworks as tunable scaffolds for chemical reactions. In particular, COFs have emerged as viable platforms for mimicking natural photosynthesis. However, there is an indisputable need for efficient, stable, and economical alternatives for the traditional platinum-based cocatalysts for light-driven hydrogen evolution. Here, we present azide-functionalized chloro(pyridine)cobaloxime hydrogen-evolution cocatalysts immobilized on a hydrazone-based COF-42 backbone that show improved and prolonged photocatalytic activity with respect to equivalent physisorbed systems. Advanced solid-state NMR and quantum-chemical methods allow us to elucidate details of the improved photoreactivity and the structural composition of the involved active site. We found that a genuine interaction between the COF backbone and the cobaloxime facilitates recoordination of the cocatalyst during the photoreaction, thereby improving the reactivity and hindering degradation of the catalyst. The excellent stability and prolonged reactivity make the herein reported cobaloxime-tethered COF materials promising hydrogen evolution catalysts for future solar fuel technologies.



INTRODUCTION

Identifying competitive alternatives to fossil-fuel-based energy constitutes one of the main research goals of this decade. Nature-inspired processes, like artificial photosynthesis, guide the way to a green and sustainable solution.^{1–3} Covalent organic frameworks (COFs) have been emerging as new materials in this context.^{4,5} COFs consist of light elements only, and their bottom-up synthesis enables high versatility and tunability on a molecular level, while benefiting from high stability and crystallinity due to covalent bonding in-plane and π - π -stacking out-of-plane.^{6–9} Most reports of COFs as photosensitizers for light-driven hydrogen evolution use platinum as a cocatalyst;^{10–12} hydrogen evolution rates up to 16.3 mmol h⁻¹ g⁻¹ have been reported in this context.¹³ Recent studies showed that the precious metal platinum can be replaced by earth-abundant molecular cocatalysts, namely, chloro(pyridine)cobaloxime and related complexes.^{14–16} These cocatalysts are well-known and well-defined, while offering high tunability, which facilitate their incorporation into photoactive organic and inorganic systems.^{17–19} Cobaloximes feature low overpotential for the hydrogen evolution reaction and have been used in heterogeneous systems with metal–organic frameworks^{20,21} and carbon nitrides,^{22,23} as well as physisorbed to COFs.¹⁴ A major drawback of molecular proton

reduction catalysts physisorbed to photosensitizers is their photodeactivation over time^{24–26} and rate limitations due to diffusion-controlled mechanisms. While previous attempts¹⁴ used molecular cobaloxime catalysts in solution, in this work we report photocatalytic hydrogen evolution with molecular cobaloxime catalysts covalently tethered to the COF backbone, yielding unprecedented insights into the nature of the active site and the COF–cocatalyst interface. By comparison with equivalent unbound, i.e., physisorbed, systems, we show how the modification of the hydrazone-based COF-42 and attachment of functionalized chloro(pyridine)cobaloxime lead to more efficient hydrogen evolution in a water/acetonitrile mixture under visible-light illumination in the presence of a sacrificial electron donor. The structural composition of the photoreaction is verified by computational and experimental methods including advanced high-resolution solid-state NMR

Received: February 28, 2020

Published: June 20, 2020



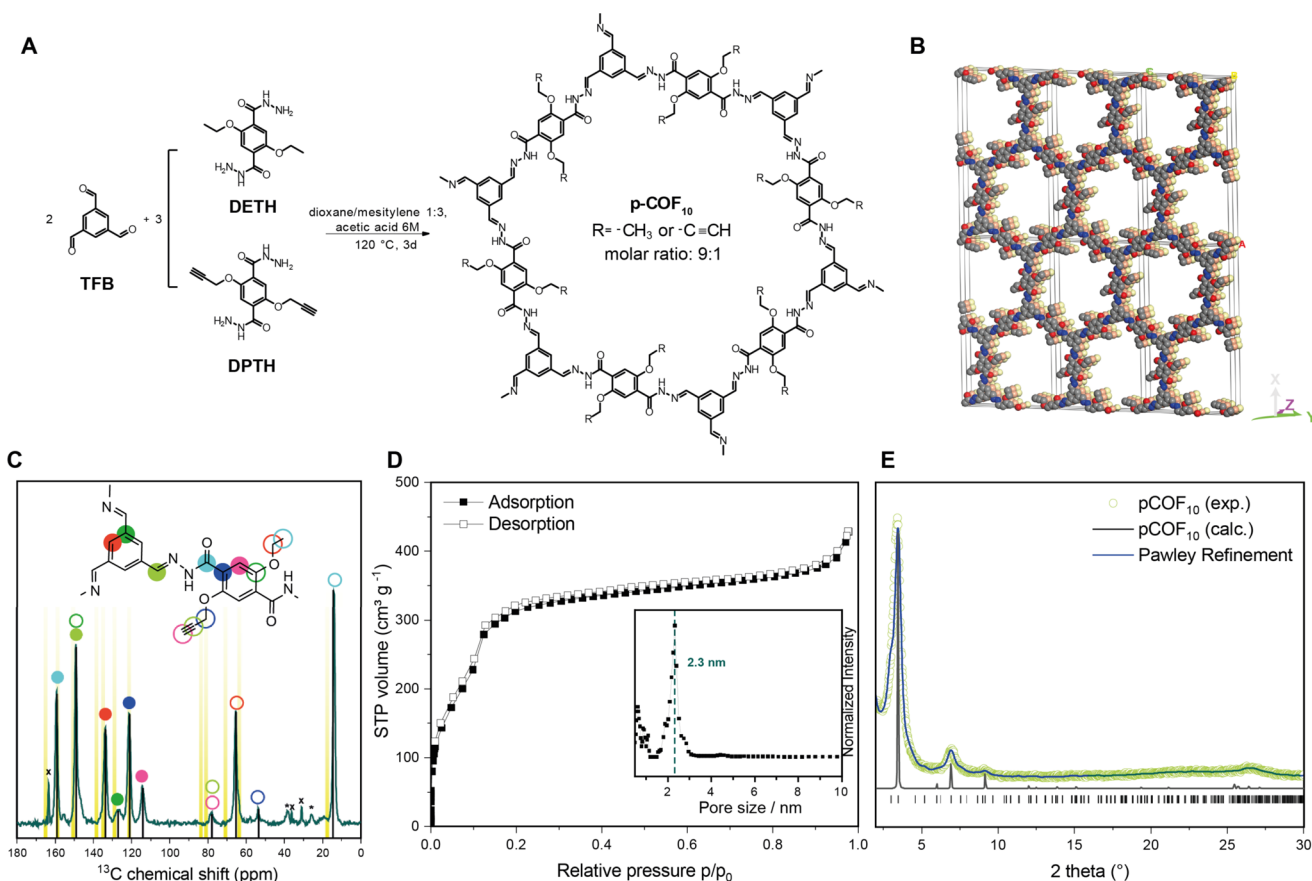


Figure 1. (A) Synthesis of pCOF₁₀ by solvothermal condensation of TFB and a 9:1 mixture of DETH and DPTH. (B) Eclipsed stacking model for pCOF₁₀. C, N, and O atoms are represented in gray, blue, and red, respectively. H atoms are omitted, and the second and third layers are represented in orange and yellow for clarity. (C) Solid-state 1D ¹³C{¹H} CP-MAS NMR spectrum of pCOF₁₀ acquired at 11.7 T, 12 kHz MAS, 298 K, and using cross-polarization times of 5 ms. Spinning side bands are marked with asterisks. Calculated shifts are marked with yellow bars. The narrow signals labeled with crosses at 164, 37, and 32 ppm correspond to residual dimethylformamide. (D) Argon adsorption isotherm of pCOF₁₀. Inlet: Pore size distribution from NLDFT calculations with cylindrical pores in equilibrium mode. The resulting main pore size is 2.3 nm. (E) PXRD pattern of pCOF₁₀ (open, green circles), Pawley refined profile (blue line), and calculated XRD pattern for the idealized AA stacking (black line).

techniques. These results combine the advantages of fully heterogeneous systems with the tunability of molecular cocatalysts and lead the way toward true single-site COF-based photocatalytic systems with a high level of interfacial control.

RESULTS AND DISCUSSION

In previous studies, COF-42²⁷ has been shown to be active in photocatalytic hydrogen evolution reactions with conventional hydrogen evolution cocatalysts such as platinum nanoparticles or molecular chloro(pyridine)cobaloxime.¹⁴ At the same time, this COF is a well-known and versatile platform that is chemically robust due to its hydrazone-linked structure.^{28,29} In this study, we used COF-42 as a platform for covalent postsynthetic modification with cobaloxime complexes. The synthesis of COF-42 by solvothermal acid-catalyzed condensation of 1,3,5-triformylbenzene (TFB) and 2,5-diethoxyterephthalohydrazide (DETH) followed published protocols.²⁷ In order to provide functional sites for the covalent attachment of the cocatalyst, 10 mol % of DETH was replaced by the propargyl-containing 2,5-bis(prop-2-yn-1-yloxy)-terephthalohydrazide (DPTH) to obtain the propargyl-modified pCOF₁₀. The COFs were characterized by FT-IR spectroscopy, sorption analysis, powder X-ray diffraction

(PXRD), magic-angle-spinning solid-state NMR (ssNMR), and quantum-chemical calculations.

The successful transformation of the starting materials to pCOF₁₀ was proven by the lack of a residual aldehyde stretching vibration in its FT-IR spectrum. Characteristic C=O vibrations and signals originating from the hydrazone bonds overlap at 1680 cm⁻¹ [see Figure S13 of the Supporting Information (SI)]. New vibrations emerged at 2250 cm⁻¹ that could be assigned to the propargyl groups, confirming the successful incorporation of DPTH building blocks into the COF backbone. This was further supported by a 1D ¹³C{¹H} ssNMR spectrum, where ¹³C signals at 79 and 58 ppm can be assigned to the propargyl functional group (Figure 1C). These shifts match the corresponding chemical shift of the liquid-state NMR of the DPTH linker (see the Supporting Information for experimental details) and are also confirmed by quantum-chemical calculations (see Table S3, SI).

PXRD analysis confirmed the crystalline structure of pCOF₁₀. The PXRD pattern shows a strong reflection at 3.3° 2θ, followed by smaller ones at 5.9°, 7.0°, and 9.1° and a very broad one at 26° 2θ. The experimental powder pattern was compared to a simulated one (see Figure 1E), and the diffraction peaks were assigned as the 100, 101, 200, 201, and 001 reflections, respectively. The peaks are broadened due to

small domain sizes in the COF particles, especially in the z direction, where the interlayer interactions are defined by π - π -stacking only. Different possible orientations for the propargyl functionality as well as slightly shifted AA' stacking modes lead to very similar powder patterns; due to broadening of the reflections in the experimental data, the different orientations cannot be distinguished. One of these possible structural models is shown in Figure 1B, featuring an AA stacking mode with an interlayer distance of 3.5 Å, which is typical for structurally similar COFs.^{10,30,31} Note that in the underlying structural model, one out of six DETH linkers per pore was replaced by DPTH, which results in a functionalization degree of 16.6% instead of the statistically distributed 10% in the experimentally prepared pCOF₁₀.

Pawley refinement of the structure in the idealized AA stacking mode suggests $P2/m$ symmetry. For the modeled structure, the resulting cell parameters are $a = 51.09$ Å, $b = 3.50$ Å, $c = 29.48$ Å, $\alpha = \gamma = 90.00^\circ$, and $\beta = 89.94^\circ$. Sorption analysis revealed a mesoporous structure with pore size of 2.3 nm and a Brunauer–Emmett–Teller (BET) surface area of 1839 m² g⁻¹, which matches the theoretically expected values of the structural model well (see Figure 1D).

For the covalent attachment of the cobaloxime catalyst to pCOF₁₀, a postsynthetic click-chemistry approach was chosen. The copper(I)-catalyzed Huisgen-type cycloaddition of azides and alkynes is known to be broadly applicable with high yields and a high tolerance for functional groups.^{32–36} Therefore, the pyridine, which acts as an axial cobaloxime ligand, was functionalized with an azide group to yield the para-functionalized pyridine **1a**, which forms the azide-functionalized complex [Co-1a], and likewise, the meta-functionalized analogues **1b** and [Co-1b] were synthesized, as depicted in Figure 2. Additionally, the equatorially functionalized chelating ligand **2** was synthesized as described in the Supporting Information. It forms the azide-functionalized catalyst [Co-2] by metal complexation as before. Two strategies were tested for the attachment of the cobaloxime complex to pCOF₁₀: (i) metal complexation of azide-functionalized ligands with

subsequent COF modification by click-reaction with the azide-functionalized complexes, termed route I, and (ii) COF modification by click-reaction with azide-functionalized ligands with subsequent complexation, termed route II (see the Supporting Information for experimental details). The resulting COF–cobaloxime hybrid samples are labeled as follows with the respective numbering according to Figure 2: [1a]–COF for clicked ligands and [Co-1a]–COF for COF–cobaloxime hybrid samples.

To verify the success of the tethering of the cobaloxime and the unperturbed structural integrity of the covalently modified hybrid COF–cobaloxime systems, we performed the same systematic experimental analysis as for the intact pCOF₁₀. PXRD shows that the crystallinity of the COF is preserved and the stacking mode does not change with respect to pCOF₁₀ (Figure S6, SI). Sorption analysis shows the expected reduction of the surface area according to Table S1 (SI). Pore size distributions for the clicked samples were calculated from Ar sorption isotherms, as shown in Figure S5 (SI). In all samples, the 2.3 nm pore size, as found in pCOF₁₀, is preserved with lower pore volume fraction, while additional smaller pores up to 1.9 nm occur, as seen from optimized pore models (see Figure S19, SI). FT-IR spectra display all expected vibrations of the COF, including propargyl vibrations at ca. 3300 and 2300 cm⁻¹. These vibrations are still visible in ligand-tethered samples, which hints at partial transformation. New triazole peaks are hidden in the region around 3100 cm⁻¹ due to low intensity. The success of the click-reaction was further confirmed by the reduced intensity of the propargyl signals relative to the other signals in the 1D ¹³C{¹H} CP ssNMR spectrum upon addition of the azide compounds. We did not observe any additional signals arising from the clicked compound, which is probably due to signal superposition, especially in the aromatic region, and due to lower signal intensity caused by a low functionalization degree. UV–vis diffuse reflectance spectra show two additional broad absorption bands at 500 and 600 nm for the cobaloxime-containing samples (Figure S15, SI). These bands are due to the electronic transitions of the azide-functionalized cobaloximes. Depending on the reaction conditions (see the Supporting Information for more details), the cobaloxime loading can be adjusted within limits. For all samples, the total cobaloxime amount was determined by ICP analysis, and for [Co-1a]–COF, it was additionally confirmed by fast-MAS ¹H-detected NMR spectra. The values range from 0.47 to 2.4 wt % for route II, while route I resulted in higher cobaloxime amounts between 1.2 and 8.5 wt %. The highest cobaloxime content was found for [Co-1a]–COF, as can be seen in Table S2 (SI). The resulting functionalization degrees ranging from 2.0 to 15% are also listed there. Scanning electron microscopy shows a flower-like morphology for all samples. Elemental mapping showed a uniform distribution of carbon, nitrogen, oxygen, and cobalt in the samples, as can be seen in the Supporting Information.

■ SSNMR ANALYSIS OF THE COF–COBALOXIME HYBRID SYSTEMS

While powder diffraction analysis provides long-range spatial information, such as approximate interlayer separations, ssNMR provides us with short-range interatomic proximities and hints about the position of the cobaloxime inside the pore. To this end, we performed an in-depth structural analysis of the clicked samples 1a–COF and [Co-1a]–COF using ¹H-

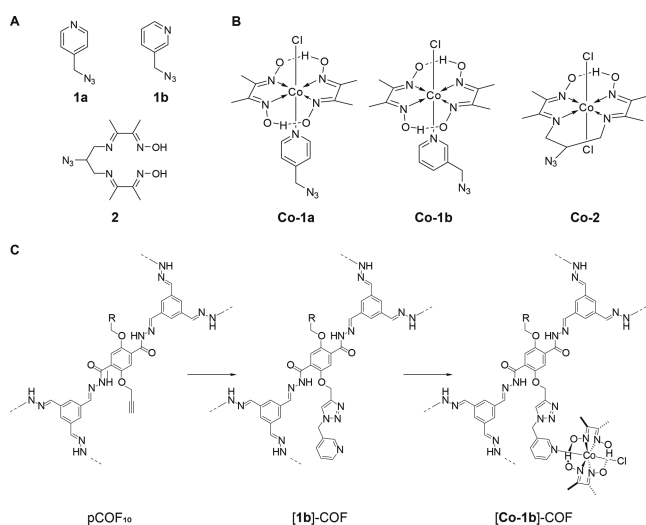


Figure 2. (A) Structure of the azide-functionalized ligands **1a**, **1b**, and **2** and (B) the azide-functionalized complexes **Co-1a**, **Co-1b**, and **Co-2**. (C) Exemplary postsynthetic COF modification toward [Co-1b]–COF. Synthesis conditions can be found in the Supporting Information.

detected, fast-MAS ssNMR at $\nu_{\text{rot}} = 55.55$ kHz at 700 MHz ^1H Larmor frequency (16.4 T). The samples based on [Co-1a] were chosen due to their higher molecular symmetry compared to that of [Co-1b]. Both 1a-COF and [Co-1a]-COF were studied by 1D and 2D ^1H and ^{13}C solid-state NMR techniques. All 2D measurements were ^1H -detected, which significantly improved the sensitivity of the natural abundance ^{13}C measurements. In addition to the sensitivity gain, we could exploit the ^1H chemical shifts as well as the ^1H - ^1H correlations as sources of structural information.

Figure 3B compares the 1D ^1H spectra of 1a-COF (yellow) and [Co-1a]-COF (blue). The high structural order of these

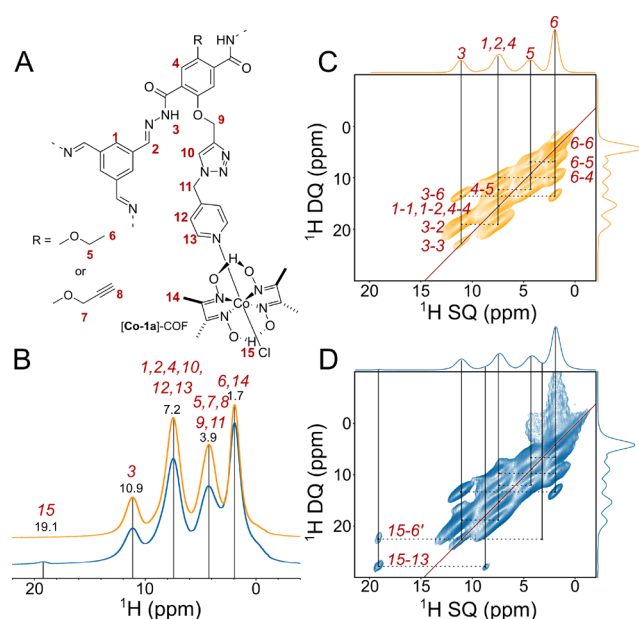


Figure 3. Solid-state NMR comparison of the ^1H spectra of [1a]-COF (yellow) and [Co-1a]-COF (blue) measured at 700 MHz ^1H Larmor frequency at $\nu_{\text{rot}} = 55.55$ kHz. (A) Schematic structure of the subsection of [Co-1a]-COF with proton labeling. (B) 1D ^1H spectra of [1a]-COF (yellow) and [Co-1a]-COF (blue). Distinct ^1H resonances are given in ppm and labeled with the corresponding atom labels as displayed in part A. (C and D) ^1H - ^1H DQ-SQ correlation spectra of [1a]-COF (yellow) and [Co-1a]-COF (blue). Horizontal dashed lines indicate the ^1H - ^1H connectivities, and vertical solid lines reflect the individual ^1H SQ resonances. Assignments are given next to the dashed lines. In part D, the assignments for only the two new connectivities are shown. The skyline projection of both dimensions is also shown.

two-dimensional crystalline polymers is reflected in the good resolution of the ^1H signals; ^1H line widths vary between 800 and 1300 Hz for 1a-COF and between 1000 and 2000 Hz for [Co-1a]-COF. In the ^1H spectra, we could directly observe four (1a-COF) and five ([Co-1a]-COF) distinct proton resonances, which correspond to the amide proton (10.9 ppm), aromatic protons overlapping with the olefin proton (7.2 ppm), methylene protons (3.9 ppm), and methyl protons (1.7 ppm). For [Co-1a]-COF, we also observe a well-separated, downfield-shifted, low-intensity peak that belongs to the strongly hydrogen-bonded oxime proton (19.1 ppm). Note that all ^1H signals are broader in the spectrum of [Co-1a]-COF relative to that of 1a-COF, which indicates that the cobaloxime functionalization process disrupted the overall COF crystallinity to some extent. Cobaloxime contains

Co(III), which is, unlike Co(II), diamagnetic; therefore, the observed line broadening of [Co-1a]-COF cannot be a consequence of paramagnetic relaxation enhancement. Also, residual CoCl_2 salt is washed out during the sample preparation process. It is more likely that the postsynthetic modification reduced the crystalline domain size and increased the sample's heterogeneity, leading to a wider range of chemical shifts for each site.

The good ^1H resolution of the fast-MAS ^1H spectrum prompted us to measure 2D homonuclear correlation experiments to gain a deeper insight into the intramolecular interaction between the COF backbone and the cobaloxime cocatalyst. We probed the relative ^1H - ^1H distances using 2D double quantum-single quantum (DQ-SQ) correlation experiments employing the R-symmetry-based $\text{R}14_4^{-2}$ homonuclear recoupling sequence.³⁷ The $\text{R}14_4^{-2}$ is a γ -encoded symmetry sequence that suppresses all heteronuclear dipole-dipole couplings and chemical shift terms in the first-order Hamiltonian. We used a $R = \pi_0$ element as the basic R-symmetry block with a nutation frequency of 97.22 kHz ($3.5\nu_{\text{rot}}$). The homonuclear 2D ^1H - ^1H DQ-SQ recoupling experiment relies on the generation of double-quantum coherences via homonuclear dipole-dipole coupling to obtain through-space information on nearby protons. Due to the double-quantum filter, the spectrum exhibits cross-peaks only between protons that share direct dipolar interactions with each other, and thus, no relayed magnetization transfer occurs. For protonated organic solid materials, such as the COFs of this study, the observation of a DQ peak is indicative of a proton-proton proximity that is ≤ 3.5 Å.^{38,39} The relative signal intensities could well approximate interatomic distances.³⁹

Parts C and D of Figure 3 show the ^1H - ^1H DQ-SQ correlation spectra of 1a-COF (yellow) and [Co-1a]-COF (blue). The spectra reveal double-quantum correlations between both distinct and identical environments, appearing at the off-diagonal and diagonal positions, respectively. Diagonal peaks are expected for the signals of the methyl and methylene groups, as well as between the resonances of the chemically equivalent aromatic sites. However, the weak diagonal peak for the NH protons corresponds to an NH-NH autopeak, which is indicative of the dipolar interaction between COF layers; the separation of NH protons within one layer is < 7 Å, while the layer-to-layer distance is 3.5 Å according to powder crystal analysis. The two spectra look almost identical, the only considerable difference being the ^1H cross-peaks of the oxime ^1H at 19.1 ppm with resonances at 8.7 and 3.4 ppm. In order to assign these two peaks, and thus uncover the position of cobaloxime inside the pore, we performed a detailed quantum-chemical study (*vide infra*). On the basis of these studies, we conclude that the resonances at 8.7 and 3.4 ppm belong to the pyridine aromatic proton (H13), as well as to a downfield-shifted methyl proton of a neighboring ethoxy group with which the cobaloxime is in close contact.

Next, we assessed the relative flexibility of the two compounds using 1D ^{13}C NMR spectroscopy. Three different 1D ^{13}C MAS spectra of [1a]-COF and [Co-1a]-COF are given in parts A and B of Figure 4, respectively. These spectra include $^{13}\text{C}\{^1\text{H}\}$ cross-polarization (CP) MAS and T_1 -weighted, direct-polarization (DP) ^{13}C spectra recorded with short (1 s) and long (25 s) recycle delay times. These latter spectra were used to elucidate the relative mobility of certain sites in the COF samples. In the ^{13}C spectra recorded with

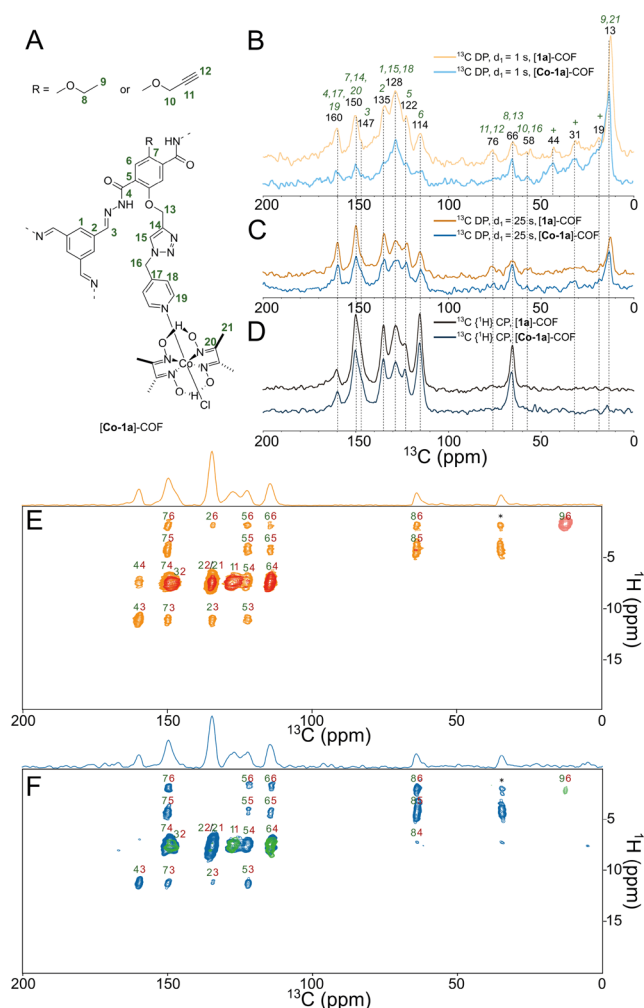


Figure 4. (A) Schematic structure of the subsection of [Co-1a]-COF with carbon labeling. (B–D) Comparison of the natural abundance ^{13}C one-dimensional solid-state NMR spectra of [1a]-COF (blue shades) and [Co-1a]-COF (orange shades) measured at 700 MHz ^1H Larmor frequency at $\nu_{\text{rot}} = 55.55$ kHz. Direct polarization spectra recorded with $d_1 = 1$ s (B) or with long $d_1 = 25$ s (C) are compared with CP MAS spectra (D). For the CP MAS experiment, the carrier was centered at 130 ppm and the CP was optimized to transfer magnetization to the aromatic region. The CP contact time was 500 μs . Signals with short longitudinal relaxation times are enhanced in the ^{13}C direct MAS spectrum measured with 1 s recycle delay. The assignment of the ^{13}C resonances was obtained from 2D ^1H - ^{13}C and ^1H - ^1H correlation experiments and from the quantum-chemical calculations. The signals marked with crosses correspond to impurities, e.g., to residual solvent signals. ^1H -detected 2D ^1H - ^{13}C correlation spectra of [1a]-COF (E) and [Co-1a]-COF (F) recorded with 500 μs (red and green) or with 2250 μs (orange and blue) CP contact times. The CP-based spectra are overlaid with INEPT-based HSQC spectra that show only one methyl cross-peak displayed with blue (E) and magenta (F) colors. For each cross-peak, the ^1H and ^{13}C assignments are displayed with red and green colors, respectively. Signals marked with an asterisk are measurement artifacts and they do not appear in 1D ^{13}C -detected $^{13}\text{C}\{^1\text{H}\}$ CP spectra.

$d_1 = 1$ s, those signals that have considerably shorter ^{13}C longitudinal relaxation time constants ($T_1 < 1$ s) are more intense, since the signal recovery is proportional to $1 - \exp(-d_1/T_1)$. Such a short T_1 is indicative of motions occurring on the inverse of the Larmor frequency (a few nanoseconds). The longitudinal relaxation constant depends

not only on the amplitude of nanosecond time-scale motion but also on the number of directly attached protons: the more protons that are directly bound to a carbon, the faster it relaxes via heteronuclear dipolar relaxation. This is reflected in the relative change of signal intensities among the aromatic carbons. Besides, the methyl resonance relaxes rapidly due to the free rotation around the C–C axis in the ethyl group. The methyl resonance line shape in the DP spectrum of [Co-1a]-COF is markedly distorted, presenting a shoulder at lower resonances. This signal could be assigned to the methyl carbons of the cobaloxime ligand. Otherwise, the signals of the covalently tethered ligand do not show any obvious sign of increased fast time-scale flexibility, neither for [1a]-COF nor for [Co-1a]-COF. In the spectrum of [Co-1a]-COF recorded with $d_1 = 1$ s, the intensified resonances at 128 ppm indicate rather flexible aromatic sites, but due to strong overlaps in this region, we could not identify if this signal belongs to the ligand or to some residual impurities that tend to show up more strongly in T_1 -weighted experiments. Selective ^{13}C or ^{15}N labeling at specified positions of the ligand would help us to quantify the amplitude and time-scale of the ligand motion.

The apparent lack of high-amplitude fast time-scale dynamics of the two COF frameworks was further validated by comparing ^1H -detected 2D CP-based ^1H - ^{13}C correlation spectra with INEPT-based 2D HSQC spectra (Figure 4D, E). High-amplitude nanosecond time-scale motion results in inherent decoupling and thus leads to increased coherent lifetimes in INEPT-based experiments and to decreased transfer efficiencies in CP-based experiments. In the HSQC spectrum of both [1a]-COF and [Co-1a]-COF, we observe only a single methyl peak, indicating that the COF backbone is generally rigid on the nanosecond time-scale.

COMPUTATIONAL STUDIES

In order to provide a structural model for the position and the orientation of the covalently tethered cobaloxime cocatalyst inside the pore, we conducted a detailed *in silico* structural investigation of [1a]-COF and [Co-1a]-COF. Atom positions and lattices of the periodic COF structure of [1a]-COF were optimized at the RI-PBE-D3/def2-TZVP^{40–43} level of theory using an acceleration scheme based on the resolution of the identity (RI) technique and the continuous fast multipole method (CFMM)^{44–46} implemented^{47,48} in Turbomole ver. V7.1.⁴⁹ The obtained structure for the [1a]-COF was then used to prepare parameters for molecular dynamics simulations using antechamber.⁵⁰ Force field minimizations and subsequent dynamics were performed with the NAMD program package^{51,52} using GAFF parameters⁵³ afterward. NMR chemical shifts were then calculated at the B97-2/pcSseg-1^{54,55} level of theory using the FermiONS++^{56,57} program package, using cut models of obtained structures to compare with experimental chemical shifts and to assign the resonances.

Using this data, we prepared 200 *in silico* ^1H - ^1H DQ–SQ and ^1H - ^{13}C 2D correlation spectra (see the Supporting Information for details) and used them to identify features that are also present in the experimentally obtained ssNMR spectra. Such features include the number of cross-peaks, especially cross-peaks of the oxime proton, their relative intensity ratios, and their peak positions. The most distinctive factor in the simulated ^1H - ^1H DQ–SQ spectra is the presence of oxime (H15) cross-peaks with resonances at around 8.7 and 3.4 ppm,

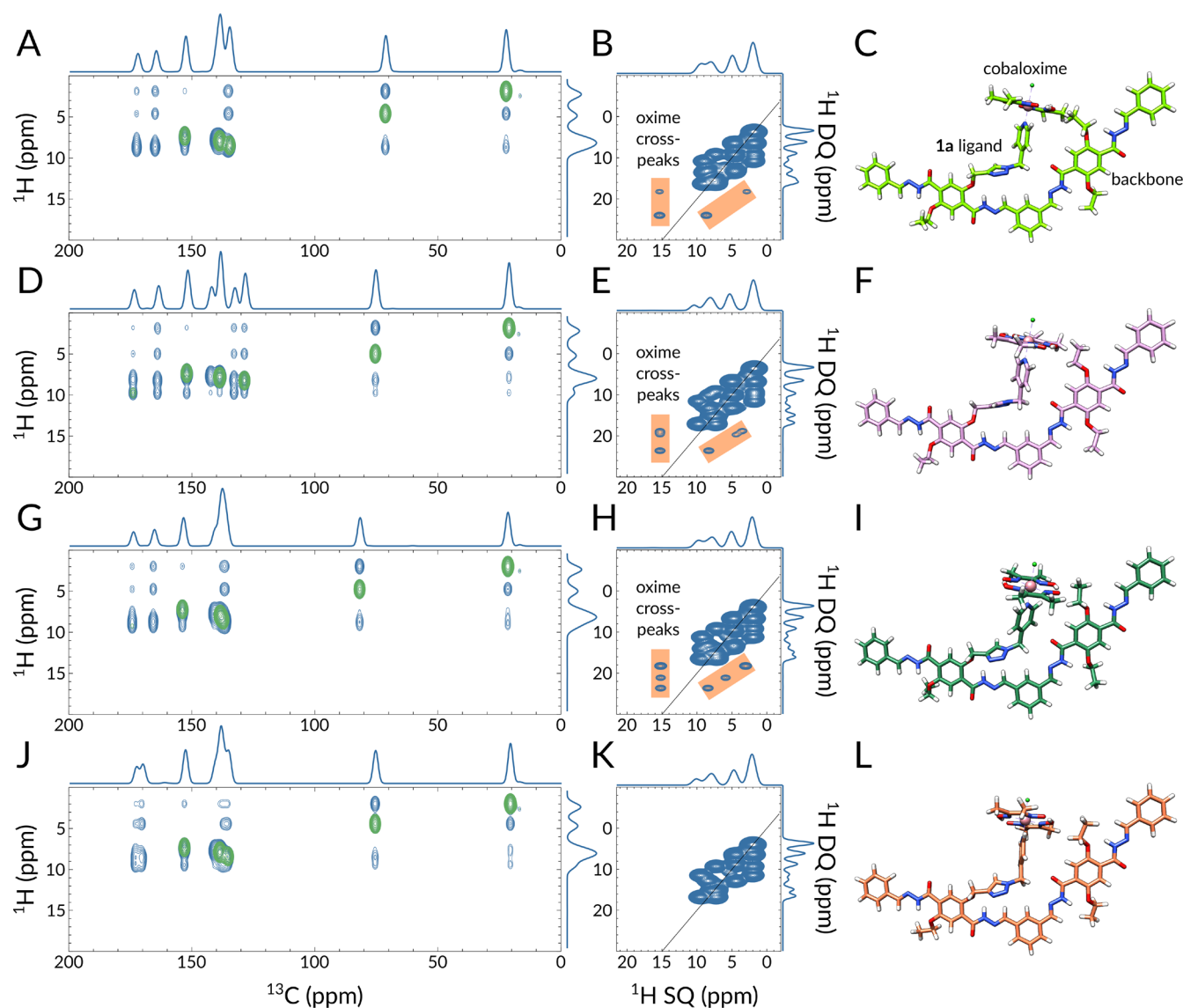


Figure 5. Direct comparison of quantum-chemically obtained ^1H - ^{13}C (A, D, G, J) and ^1H - ^1H DQ-SQ (B, E, H, K) 2D ssNMR spectra with corresponding structural models of [Co-1a]-COF on the right (C, F, I, L). For a better comparison, the same NMR chemical shift region is displayed as in the experimentally obtained spectra (Figures 3C,D and 4D,E). In the ^1H - ^{13}C 2D spectra, blue and green colors represent ^1H - ^{13}C atom pairs that are within 6 and 2 Å, respectively. In the ^1H - ^1H DQ-SQ spectra, the orange color highlights the oxime proton cross-peaks. In parts C, F, I, and L, the Co, Cl, O, N, and H atoms are displayed in pink, lime, red, blue, and white, respectively.

which was used to categorize the simulated spectra. These distinct chemical shifts suggest that the oxime proton is interacting with an aromatic proton (at 8.7 ppm) and with either an upfield-shifted methylene proton or with a downfield-shifted methyl proton (at 3.4 ppm). There are four different aromatic protons in [Co-1a]-COF, H1, H4, H12, and H13, out of which only H4 and H13 can get closer than 3.5 Å to H15.

To decide which resonance leads to the 3.4 ppm cross-peak with H15, we analyzed the shielding effects of the glyoxime group on the nearby ethoxy methyl and methylene protons. The approach of the glyoxime oxygen toward the ethoxy group induces a deshielding effect; consequently, both the methyl and the methylene protons resonate at higher frequencies (see Figure S16 and SI text for more details), this rules out the possibility that the cross-peak at 3.4 ppm would stem from an upfield-shifted methylene proton and leaves only a downfield-shifted methyl proton as a possible interaction partner. Besides,

we excluded the possibility that the oxime proton shows a trivial intraligand cross-peak with the glyoxime methyl protons, since (i) the distance between the H15 and H16 protons is >3.5 Å and (ii) the calculated chemical shift is below 2.9 ppm.

Out of the 200 simulated ^1H - ^1H DQ-SQ spectra, 27 (13) contained two (three) oxime cross-peaks, among which 22 spectra have these peaks in the expected ppm range. By considering the relative peak intensity ratios between the oxime cross-peaks, only 15 spectra have a more intense aromatic-oxime than a methyl-oxime cross-peak. Two such spectra, together with the simulated ^1H - ^{13}C spectra and corresponding structures, are displayed in Figure 5A-F. As counter-examples, Figure 5G,H and J,K displays the spectra of such structures (Figure 5I and L) where three equally intense peaks (Figure 5H) or no oxime proton cross-peak (Figure 5K) appears in the simulated DQ-SQ spectra. The possibility that, in reality, in a fraction of the [Co-1a]-COF pores the cobaloxime does not interact with the pore wall cannot be

ruled out; nonetheless, our current data suggest that when it does, it gets in close contact with the nearby ethoxy group. It is also likely that this genuine interaction stabilizes the complex and restricts the cocatalyst's degradation during the photocatalytic cycles. Note that, at this stage, both the ssNMR measurements and the *in silico* calculations were performed in a solvent-free environment. Future ssNMR measurements with added acetonitrile/water mixture accompanied by simulations in explicit solvent could reveal if the cobaloxime stays attached to the pore wall or whether it gains more flexibility and drifts toward the pore center.

To inspect the spacial arrangement inside the pore, we modeled [Co-1a]-COF including one tethered cocatalyst based on the MD-simulated structures (Figure 6). The

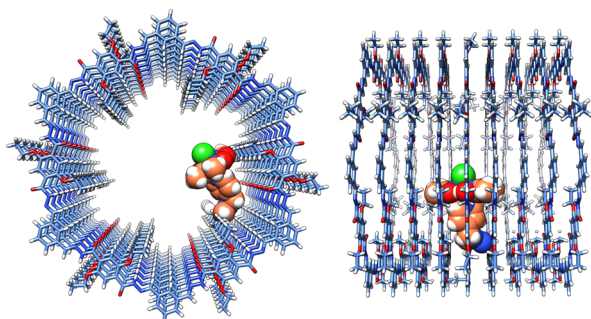


Figure 6. Front and side views of the MD-simulated structural model of [Co-1a]-COF showing a possible arrangement of the cocatalyst. The linker and the cobaloxime group are depicted by spheres and their carbon atoms are displayed in orange. Co, Cl, O, N, and H atoms are displayed in pink, lime, red, blue, and white, and C atoms of the backbone are light blue.

displayed ligand has the same orientation as in Figure 5C. From the side and front views it is apparent that the ligand spreads over multiple layers and occupies a substantial portion of the pore. Due to spacial confinements, our model suggests that no more than three [Co-1a] over three layers can fit into the backbone; i.e., the maximum number of [Co-1a] per layer is one. In our case, we have 13 mol % functionalization, which translates into one [Co-1a] for every seven layers.

PHOTOCATALYTIC ACTIVITY

To probe whether there is a possible benefit of covalent cocatalyst immobilization over simple physisorption,^{14,15} the COF-cobaloxime hybrid samples were tested for photocatalytic activity. In a typical photocatalysis experiment, 5 mg of COF hybrid was suspended in 10 mL of acetonitrile and water in a ratio of 4:1 at pH 8 containing 100 μ L of triethanolamine (TEOA) as sacrificial donor. A housed Xe lamp was used to illuminate the suspension interface with a nominal beam spectral distribution similar to that of AM1.5G. The beam intensity before experiments was then adjusted to 100 mW cm^{-2} . See the SI for more details. Photocatalytic hydrogen evolution reaction (HER) rates were quantified in a continuous flow reactor as previously reported¹⁵ (Figure 7A). As a reference system, we compared the hybrid systems to samples where [Co-1a] or [Co-1b] was added to the suspension and physisorbed to COF-42 with a BET surface area of 2336 $\text{m}^2 \text{g}^{-1}$ during photocatalysis. The maximum photonic efficiencies after *in situ* photoactivation of the samples ranging from 2 to 8 wt % cobaloxime catalyst according to ICP results can be found in Figure 7A. In the physisorbed samples, an increase of the photonic efficiency was found when increasing the catalyst amount from 2 to 4 wt % with a maximum efficiency of 0.06% for [Co-1a] and 0.07% for [Co-1b] at 4.0 wt %, while the efficiency is fairly constant at higher percentages (0.06%–0.08% at 5.0 and 8.0 wt %) for [Co-1b]. This behavior is expected for the system; as in the low-loading region, the photocatalytic activity scales linearly with the cocatalyst amount, while it reaches a maximum in the higher-loading region where the availability of the cocatalyst is not limiting anymore.

In the hybrid samples, an activity maximum rather than a constant behavior is found for each hybrid type. For the para-functionalized [Co-1a], the highest photonic efficiency was found at 4.1 wt %, while for the meta-functionalized [Co-1b] the maximum was found at 3.2 wt %. As before, a linear increase of the photonic efficiency in the low-loading regime was observed. However, a further increase in cobaloxime loading resulted in lower activity in the immobilized samples. We attribute this to a predominant pore-clogging effect of the active sites with increasing functionalization. In general, the highest photonic efficiency was achieved with [Co-1a]-COF at 0.14% followed by [Co-1b]-COF at 0.11%. Compared to the physisorbed samples with the corresponding cobaloxime

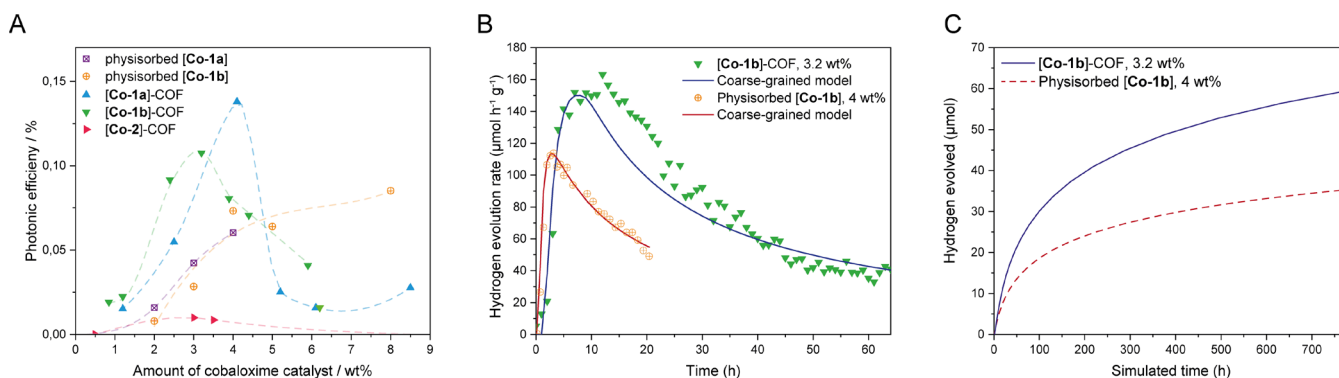


Figure 7. (A) Comparison of photonic efficiencies for hybrid samples and COF-42 with physisorbed [Co-1a] and [Co-1b]. (B) Comparison of the hydrogen evolution rate of [Co-1b]-COF containing 3.2 wt % [Co-1b] and COF-42 with 4.0 wt % physisorbed [Co-1b] and coarse-grained model fits of both systems. (C) Projection of the hydrogen evolution of [Co-1b]-COF containing 3.2 wt % [Co-1b] and COF-42 with 4.0 wt % physisorbed [Co-1b] based on the coarse-grained models.

content, the activity doubles for both systems. Additionally, to emphasize the role of the complex environment of the cobaloxime over the pure presence of Co(II), we performed a measurement where we added CoCl_2 to a suspension of pCOF_{10} and triethanolamine in the photocatalysis medium, as well as experiments where one of the components (COF, TEOA) was excluded (see Supporting Information). None of the reference samples showed hydrogen evolution after several hours of irradiation. For the hybrid samples, the close contact between the cobaloxime and the COF pore wall—revealed by representative solid-state NMR and computational studies (*vide supra*) with [Co-1a]–COF—might facilitate charge transfer to the cobaloxime catalyst from the COF pore wall, as also observed from photoluminescence measurements (see Figures S11 and S12, SI) where [Co-2]–COF shows a significantly lower activity in $\text{CH}_3\text{CN}/\text{H}_2\text{O}$, which is a known effect for cobaloximes that lack equatorial protons. The protonation of the oxime oxygen, which is necessary for the catalytic process, is hindered in those cases.^{58,59} The catalytic activity could not be improved by lowering the pH to 4. In this case, different acids (ascorbic acid, acetic acid, and citric acid) were tested that simultaneously served as sacrificial electron donors instead of the amine base TEOA. Even though the stability of [Co-2]–COF is predicted to be higher than that for the other tested cobaloximes, the complex proved not to be appropriate in our case. We compared the best performing [Co-1b]–COF sample (containing 3.2 wt % cobaloxime) to COF-42 physisorbed with [Co-1b]. A sample with the same amount of physisorbed cobaloxime was qualitatively active in photocatalytic hydrogen evolution, but for precise quantification, we increased the catalyst amount to 4.0 wt %. Even though it contained 20% less catalyst, the hybrid sample was 47% more active than the physisorbed one (163 vs 111 $\mu\text{mol h}^{-1} \text{g}^{-1}$) (see Figure 7A). Additionally, the long-term stability increased significantly. After 20 h, the physisorbed sample shows 52% of its initial activity, while the hybrid sample maintains 80% of its initial activity. To get an estimate of the longevity of the systems, we fitted the hydrogen evolution rates of both samples with a coarse-grained model (Figure 7C) that was established in an earlier study on photocatalysis with COFs and a nickel-based oligomer as cocatalyst.¹⁵ The model resulted in very precise fitting for the physisorbed catalyst because of similarities to the original nickel-based system from where the coarse-grain fitting model was obtained, while the hybrid sample showed a more complex behavior that is not perfectly mapped with this simplified model. On the basis of the coarse-grained fits, we projected the total amount of hydrogen evolved by the samples at full depletion (see Figure 7C). After 780 h, the projection of the physisorbed sample reaches 35 μmol of hydrogen evolved, while the value is 59 μmol for the hybrid sample, which is a gain of 69%. Comparing the estimated turnover numbers (TONs) of both systems, the deviation gets even more obvious. While the TON after 780 h is simulated to be 81 for the physisorbed sample, it increases by 110% to a value of 170 in the hybrid sample. We attribute this activity enhancement to the local confinement in the COF hybrid samples, as supported by MD simulations.

Cobaloximes are known to slowly decompose under photocatalytic conditions. The labile axial pyridine ligand decoordinates in the catalytic cycle due to a square-planar Co(II) transition state. The catalyst in solution can then possibly be reduced, which limits its stability. Due to the

confinement between the ligand and catalyst in the COF pores, the recoordination might be enhanced, hence counteracting degradation, which leads to reactivation of the catalyst. Additionally, charge transfer is favored in the case of the spatial proximity of the cocatalyst and the pore wall. Both effects result in higher overall activity as well as longevity. Interestingly, the activation period for the hybrid samples is significantly longer than for the physisorbed ones. This may be attributed to the time-delayed accessibility of the catalyst in the pores. Both limitations could be addressed via a method that was recently published by Thomas and co-workers,^{60,61} where silica spheres were used to create an inverse-opal architecture in the COF material. The so created macropores could serve as channels for reagents and products. Also, immobilization of the cocatalyst in a COF with larger pores might have a similar effect.

CONCLUSION

In summary, we have developed a platform derived from COF-42 as a support for the immobilization of cobaloxime catalysts. The postsynthetic modification of propargyl-functionalized COF-42 enabled the covalent tethering of three different cobaloximes to form COF–cobaloxime hybrid systems. This tethering significantly enhanced the photocatalytic activity of the system by more than 100% compared to that of the physisorbates with the corresponding cobaloxime amount. The high crystallinity of our materials allowed for an in-depth solid-state 2D NMR characterization using fast MAS and proton detection. In the 1D ^1H spectrum of [Co-1a]–COF, we could clearly identify the resonance corresponding to the oxime proton on the basis of its highly downfield-shifted resonance. The 2D ^1H – ^1H DQ–SQ experiment showed two cross-peaks for the oxime proton, consistent with the incorporation of the cocatalyst into the COF material. MD simulations with subsequent quantum-chemical NMR chemical shift calculations allowed us to locate the position of the tethered ligand inside the pore on the basis of the experimentally observed oxime proton cross-peaks. Our analysis suggests that the cobaloxime in [Co-1a]–COF closely interacts with the pore wall. We surmise that this interaction is responsible both for the improved photocatalytic activity and for the prolonged activity of the hybrid samples with respect to the physisorbed variant. We anticipate that larger pore channels or the addition of dedicated transport pores will further improve the pore accessibility and prevent back-reaction via local confinement of the products, thereby increasing the hydrogen evolution activity of the system even further.

ASSOCIATED CONTENT

Supporting Information

The Supporting Information is available free of charge at <https://pubs.acs.org/doi/10.1021/jacs.0c02155>.

Experimental procedures, COF synthesis, and details of molecular dynamic simulations, quantum-chemical calculations, and additional measurements (PDF)

AUTHOR INFORMATION

Corresponding Author

Bettina V. Lotsch – Max Planck Institute for Solid State Research, 70569 Stuttgart, Germany; Department of Chemistry, University of Munich (LMU), 81377 Munich, Germany; Cluster of Excellence e-conversion, 85748 Garching, Germany;

Center for Nanoscience (CeNS), 80799 Munich, Germany;
orcid.org/0000-0002-3094-303X; Email: b.lotsch@
fkf.mpg.de

Authors

Kerstin Gottschling – Max Planck Institute for Solid State Research, 70569 Stuttgart, Germany; Department of Chemistry, University of Munich (LMU), 81377 Munich, Germany; Cluster of Excellence e-conversion, 85748 Garching, Germany; Center for Nanoscience (CeNS), 80799 Munich, Germany

Gökçen Savasci – Max Planck Institute for Solid State Research, 70569 Stuttgart, Germany; Department of Chemistry, University of Munich (LMU), 81377 Munich, Germany; Cluster of Excellence e-conversion, 85748 Garching, Germany; Center for Nanoscience (CeNS), 80799 Munich, Germany;
orcid.org/0000-0002-6183-7715

Hugo Vignolo-González – Max Planck Institute for Solid State Research, 70569 Stuttgart, Germany

Sandra Schmidt – Department of Chemistry, University of Munich (LMU), 81377 Munich, Germany; orcid.org/0000-0003-3972-9459

Philipp Mauker – Department of Chemistry, University of Munich (LMU), 81377 Munich, Germany; Center for Nanoscience (CeNS), 80799 Munich, Germany

Tanmay Banerjee – Max Planck Institute for Solid State Research, 70569 Stuttgart, Germany; orcid.org/0000-0002-4548-2117

Petra Rovó – Department of Chemistry, University of Munich (LMU), 81377 Munich, Germany; Center for Nanoscience (CeNS), 80799 Munich, Germany; orcid.org/0000-0001-8729-7326

Christian Ochsenfeld – Department of Chemistry, University of Munich (LMU), 81377 Munich, Germany; Max Planck Institute for Solid State Research, 70569 Stuttgart, Germany; Cluster of Excellence e-conversion, 85748 Garching, Germany; Center for Nanoscience (CeNS), 80799 Munich, Germany;
orcid.org/0000-0002-4189-6558

Complete contact information is available at:
<https://pubs.acs.org/10.1021/jacs.0c02155>

Notes

The authors declare no competing financial interest.

ACKNOWLEDGMENTS

Financial support is gratefully acknowledged from the Max Planck Society, an ERC Starting Grant (project COF Leaf, grant number 639233), the Deutsche Forschungsgemeinschaft (DFG) via the SFB 1333 (project A03), the Cluster of Excellence e-conversion, and the Center for Nanoscience. P.R. acknowledges the Deutsche Forschungsgemeinschaft (DFG, German Research Foundation) SFB 1309-325871075, project A3, and Fonds der Chemischen Industrie. We thank Prof. T. Bein and Prof. W. Schnick (University of Munich, LMU) for granting access to the XRD facility and V. Duppel and M.-L. Schreiber for the assistance with material analysis.

REFERENCES

(1) Li, L.; Cai, Z.; Wu, Q.; Lo, W.-Y.; Zhang, N.; Chen, L. X.; Yu, L. Rational Design of Porous Conjugated Polymers and Roles of Residual Palladium for Photocatalytic Hydrogen Production. *J. Am. Chem. Soc.* **2016**, *138*, 7681–7686.

(2) Zhang, Y.; Mao, F.; Wang, L.; Yuan, H.; Liu, P. F.; Yang, H. G. Recent Advances in Photocatalysis over Metal–Organic Frameworks-Based Materials. *Solar RRL* **2020**, *4*, 1900438.

(3) Diercks, C. S.; Liu, Y.; Cordova, K. E.; Yaghi, O. M. The role of reticular chemistry in the design of CO₂ reduction catalysts. *Nat. Mater.* **2018**, *17*, 301–307.

(4) Vyas, V. S.; Lau, V. W.-h.; Lotsch, B. V. Soft Photocatalysis: Organic Polymers for Solar Fuel Production. *Chem. Mater.* **2016**, *28*, 5191–5204.

(5) Sick, T.; Hufnagel, A. G.; Kampmann, J.; Kondofersky, I.; Calik, M.; Rotter, J. M.; Evans, A.; Döblinger, M.; Herbert, S.; Peters, K.; Böhm, D.; Knochel, P.; Medina, D. D.; Fattakhova-Rohlfing, D.; Bein, T. Oriented Films of Conjugated 2D Covalent Organic Frameworks as Photocathodes for Water Splitting. *J. Am. Chem. Soc.* **2018**, *140*, 2085–2092.

(6) Côté, A. P.; Benin, A. I.; Ockwig, N. W.; O’Keeffe, M.; Matzger, A. J.; Yaghi, O. M. Porous, Crystalline, Covalent Organic Frameworks. *Science* **2005**, *310*, 1166.

(7) Tilford, R. W.; Mugavero, S. J.; Pellechia, P. J.; Lavigne, J. J. Tailoring Microporosity in Covalent Organic Frameworks. *Adv. Mater.* **2008**, *20*, 2741–2746.

(8) Ding, S.-Y.; Wang, W. Covalent organic frameworks (COFs): from design to applications. *Chem. Soc. Rev.* **2013**, *42*, 548–568.

(9) Lohse, M. S.; Bein, T. Covalent Organic Frameworks: Structures, Synthesis, and Applications. *Adv. Funct. Mater.* **2018**, *28*, 1705553.

(10) Stegbauer, L.; Schwinghammer, K.; Lotsch, B. V. A hydrazone-based covalent organic framework for photocatalytic hydrogen production. *Chem. Sci.* **2014**, *5*, 2789–2793.

(11) Haase, F.; Banerjee, T.; Savasci, G.; Ochsenfeld, C.; Lotsch, B. V. Structure–property–activity relationships in a pyridine containing azine-linked covalent organic framework for photocatalytic hydrogen evolution. *Faraday Discuss.* **2017**, *201*, 247–264.

(12) Stegbauer, L.; Zech, S.; Savasci, G.; Banerjee, T.; Podjaski, F.; Schwinghammer, K.; Ochsenfeld, C.; Lotsch, B. V. Tailor-Made Photoconductive Pyrene-Based Covalent Organic Frameworks for Visible-Light Driven Hydrogen Generation. *Adv. Energy Mater.* **2018**, *8*, 1703278.

(13) Wang, X.; Chen, L.; Chong, S. Y.; Little, M. A.; Wu, Y.; Zhu, W.-H.; Clowes, R.; Yan, Y.; Zwiijnenburg, M. A.; Sprick, R. S.; Cooper, A. I. Sulfone-containing covalent organic frameworks for photocatalytic hydrogen evolution from water. *Nat. Chem.* **2018**, *10*, 1180–1189.

(14) Banerjee, T.; Haase, F.; Savasci, G.; Gottschling, K.; Ochsenfeld, C.; Lotsch, B. V. Single-Site Photocatalytic H₂ Evolution from Covalent Organic Frameworks with Molecular Cobaloxime Co-Catalysts. *J. Am. Chem. Soc.* **2017**, *139*, 16228–16234.

(15) Biswal, B. P.; Vignolo-González, H. A.; Banerjee, T.; Grunenberg, L.; Savasci, G.; Gottschling, K.; Nuss, J.; Ochsenfeld, C.; Lotsch, B. V. Sustained Solar H₂ Evolution from a Thiazolo[5,4-d]thiazole-Bridged Covalent Organic Framework and Nickel-Thiolate Cluster in Water. *J. Am. Chem. Soc.* **2019**, *141*, 11082–11092.

(16) Banerjee, T.; Gottschling, K.; Savasci, G.; Ochsenfeld, C.; Lotsch, B. V. H₂ Evolution with Covalent Organic Framework Photocatalysts. *ACS Energy Letters* **2018**, *3*, 400–409.

(17) Dempsey, J. L.; Brunschwig, B. S.; Winkler, J. R.; Gray, H. B. Hydrogen Evolution Catalyzed by Cobaloximes. *Acc. Chem. Res.* **2009**, *42*, 1995–2004.

(18) Artero, V.; Chavarot-Kerlidou, M.; Fontecave, M. Splitting Water with Cobalt. *Angew. Chem., Int. Ed.* **2011**, *50*, 7238–7266.

(19) Muresan, N. M.; Willkomm, J.; Mersch, D.; Vaynzof, Y.; Reisner, E. Immobilization of the Molecular Cobaloxime Catalyst for Hydrogen Evolution on a Mesoporous Metal Oxide Electrode. *Angew. Chem., Int. Ed.* **2012**, *51*, 12749–12753.

(20) Nasalevich, M. A.; Becker, R.; Ramos-Fernandez, E. V.; Castellanos, S.; Veber, S. L.; Fedin, M. V.; Kapteijn, F.; Reek, J. N. H.; van der Vlugt, J. I.; Gascon, J. Co@NH₂-MIL-125(Ti): cobaloxime-derived metal–organic framework-based composite for light-driven H₂ production. *Energy Environ. Sci.* **2015**, *8*, 364–375.

- (21) Gao, L.-F.; Zhu, Z.-Y.; Feng, W.-S.; Wang, Q.; Zhang, H.-L. Disentangling the Photocatalytic Hydrogen Evolution Mechanism of One Homogeneous Cobalt-Coordinated Polymer. *J. Phys. Chem. C* **2016**, *120*, 28456–28462.
- (22) Cao, S.-W.; Liu, X.-F.; Yuan, Y.-P.; Zhang, Z.-Y.; Fang, J.; Loo, S. C. J.; Barber, J.; Sum, T. C.; Xue, C. Artificial photosynthetic hydrogen evolution over g-C₃N₄ nanosheets coupled with cobaloxime. *Phys. Chem. Chem. Phys.* **2013**, *15*, 18363.
- (23) Li, X.; Masters, A. F.; Maschmeyer, T. Photocatalytic Hydrogen Evolution from Silica-Templated Polymeric Graphitic Carbon Nitride-Is the Surface Area Important? *ChemCatChem* **2015**, *7*, 121–126.
- (24) Lazarides, T.; McCormick, T.; Du, P.; Luo, G.; Lindley, B.; Eisenberg, R. Making Hydrogen from Water Using a Homogeneous System Without Noble Metals. *J. Am. Chem. Soc.* **2009**, *131*, 9192–9194.
- (25) Lakadamyali, F.; Reisner, E. Photocatalytic H₂ evolution from neutral water with a molecular cobalt catalyst on a dye-sensitized TiO₂ nanoparticle. *Chem. Commun.* **2011**, *47*, 1695.
- (26) Yin, M.; Ma, S.; Wu, C.; Fan, Y. A noble-metal-free photocatalytic hydrogen production system based on cobalt(III) complex and eosin Y-sensitized TiO₂. *RSC Adv.* **2015**, *5*, 1852–1858.
- (27) Uribe-Romo, F. J.; Doonan, C. J.; Furukawa, H.; Oisaki, K.; Yaghi, O. M. Crystalline Covalent Organic Frameworks with Hydrazone Linkages. *J. Am. Chem. Soc.* **2011**, *133*, 11478–11481.
- (28) Gottschling, K.; Stegbauer, L.; Savasci, G.; Prisco, N. A.; Berkson, Z. J.; Ochsenfeld, C.; Chmelka, B. F.; Lotsch, B. V. Molecular Insights into Carbon Dioxide Sorption in Hydrazone-Based Covalent Organic Frameworks with Tertiary Amine Moieties. *Chem. Mater.* **2019**, *31*, 1946–1955.
- (29) Zhang, Y.; Shen, X.; Feng, X.; Xia, H.; Mu, Y.; Liu, X. Covalent organic frameworks as pH responsive signaling scaffolds. *Chem. Commun.* **2016**, *52*, 11088–11091.
- (30) Chen, X.; Addicoat, M.; Jin, E.; Xu, H.; Hayashi, T.; Xu, F.; Huang, N.; Irle, S.; Jiang, D. Designed synthesis of double-stage two-dimensional covalent organic frameworks. *Sci. Rep.* **2015**, *5*, 14650.
- (31) Li, Z.-J.; Ding, S.-Y.; Xue, H.-D.; Cao, W.; Wang, W. Synthesis of –C=N– linked covalent organic frameworks via the direct condensation of acetals and amines. *Chem. Commun.* **2016**, *52*, 7217–7220.
- (32) Himo, F.; Lovell, T.; Hilgraf, R.; Rostovtsev, V. V.; Noodleman, L.; Sharpless, K. B.; Fokin, V. V. Copper(I)-Catalyzed Synthesis of Azoles. DFT Study Predicts Unprecedented Reactivity and Intermediates. *J. Am. Chem. Soc.* **2005**, *127*, 210–216.
- (33) Rostovtsev, V. V.; Green, L. G.; Fokin, V. V.; Sharpless, K. B. A Stepwise Huisgen Cycloaddition Process: Copper(I)-Catalyzed Regioselective “Ligation” of Azides and Terminal Alkynes. *Angew. Chem., Int. Ed.* **2002**, *41*, 2596–2599.
- (34) Hein, C. D.; Liu, X.-M.; Wang, D. Click Chemistry, A Powerful Tool for Pharmaceutical Sciences. *Pharm. Res.* **2008**, *25*, 2216–2230.
- (35) Amblard, F.; Cho, J. H.; Schinazi, R. F. Cu(I)-Catalyzed Huisgen Azide-Alkyne 1,3-Dipolar Cycloaddition Reaction in Nucleoside, Nucleotide, and Oligonucleotide Chemistry. *Chem. Rev.* **2009**, *109*, 4207–4220.
- (36) Meldal, M.; Tornøe, C. W. Cu-Catalyzed Azide-Alkyne Cycloaddition. *Chem. Rev.* **2008**, *108*, 2952–3015.
- (37) Levitt, M. H. Symmetry-Based Pulse Sequences in Magic-Angle Spinning Solid-State NMR. In *eMagRes*; Wiley, 2007; pp 1–31.
- (38) Brown, S. P.; Lesage, A.; Elena, B.; Emsley, L. Probing Proton-Proton Proximities in the Solid State: High-Resolution Two-Dimensional 1H-1H Double-Quantum CRAMPS NMR Spectroscopy. *J. Am. Chem. Soc.* **2004**, *126*, 13230–13231.
- (39) Bradley, J. P.; Tripon, C.; Filip, C.; Brown, S. P. Determining relative proton–proton proximities from the build-up of two-dimensional correlation peaks in 1H double-quantum MAS NMR: insight from multi-spin density-matrix simulations. *Phys. Chem. Chem. Phys.* **2009**, *11*, 6941.
- (40) Perdew, J. P.; Burke, K.; Ernzerhof, M. Generalized Gradient Approximation Made Simple. *Phys. Rev. Lett.* **1996**, *77*, 3865–3868.
- (41) Grimme, S.; Antony, J.; Ehrlich, S.; Krieg, H. A consistent and accurate ab initio parametrization of density functional dispersion correction (DFT-D) for the 94 elements H-Pu. *J. Chem. Phys.* **2010**, *132*, 154104.
- (42) Schäfer, A.; Huber, C.; Ahlrichs, R. Fully optimized contracted Gaussian basis sets of triple zeta valence quality for atoms Li to Kr. *J. Chem. Phys.* **1994**, *100*, 5829–5835.
- (43) Eichkorn, K.; Weigend, F.; Treutler, O.; Ahlrichs, R. Auxiliary basis sets for main row atoms and transition metals and their use to approximate Coulomb potentials. *Theor. Chem. Acc.* **1997**, *97*, 119–124.
- (44) Burow, A. M.; Sierka, M.; Mohamed, F. Resolution of identity approximation for the Coulomb term in molecular and periodic systems. *J. Chem. Phys.* **2009**, *131*, 214101.
- (45) Grajciar, L. Low-memory iterative density fitting. *J. Comput. Chem.* **2015**, *36*, 1521–1535.
- (46) Burow, A. M.; Sierka, M. Linear Scaling Hierarchical Integration Scheme for the Exchange-Correlation Term in Molecular and Periodic Systems. *J. Chem. Theory Comput.* **2011**, *7*, 3097–3104.
- (47) Łazarski, R.; Burow, A. M.; Sierka, M. Density Functional Theory for Molecular and Periodic Systems Using Density Fitting and Continuous Fast Multipole Methods. *J. Chem. Theory Comput.* **2015**, *11*, 3029–3041.
- (48) Łazarski, R.; Burow, A. M.; Grajciar, L.; Sierka, M. Density functional theory for molecular and periodic systems using density fitting and continuous fast multipole method: Analytical gradients. *J. Comput. Chem.* **2016**, *37*, 2518–2526.
- (49) TURBOMOLE, ver. 7.1; TURBOMOLE GmbH, 2016. Available at <http://www.turbomole.com>.
- (50) Wang, J.; Wang, W.; Kollman, P. A.; Case, D. A. Automatic atom type and bond type perception in molecular mechanical calculations. *J. Mol. Graphics Modell.* **2006**, *25*, 247–260.
- (51) Phillips, J. C.; Braun, R.; Wang, W.; Gumbart, J.; Tajkhorshid, E.; Villa, E.; Chipot, C.; Skeel, R. D.; Kalé, L.; Schulten, K. Scalable molecular dynamics with NAMD. *J. Comput. Chem.* **2005**, *26*, 1781–1802.
- (52) Case, D. A.; Betz, R. M.; Cerutti, D. S.; Cheatham, T. E., III; Darden, T. A.; Duke, R. E.; Giese, T. J.; Gohlke, H.; Goetz, A. W.; Homeyer, N.; Izadi, S.; Janowski, P.; Kaus, J.; Kovalenko, A.; Lee, T. S.; LeGrand, S.; Li, P.; Lin, C.; Luchko, T.; Lu, R.; Madej, B.; Mermelstein, D.; Merz, K. M.; Monard, G.; Nguyen, H.; Nguyen, H. T.; Omelyan, I.; Onufriev, A.; Roe, D. R.; Roitberg, A.; Sagui, C.; Simmerling, C. L.; Botello-Smith, W. M.; Swails, J.; Walker, R. C.; Wang, J.; Wolf, R. M.; Wu, X.; Xiao, L.; Kollman, P. A. AMBER 2016; University of California: San Francisco, CA, 2016.
- (53) Wang, J.; Wolf, R. M.; Caldwell, J. W.; Kollman, P. A.; Case, D. A. Development and testing of a general amber force field. *J. Comput. Chem.* **2004**, *25*, 1157–1174.
- (54) Wilson, P. J.; Bradley, T. J.; Tozer, D. J. Hybrid exchange-correlation functional determined from thermochemical data and ab initio potentials. *J. Chem. Phys.* **2001**, *115*, 9233–9242.
- (55) Jensen, F. Segmented Contracted Basis Sets Optimized for Nuclear Magnetic Shielding. *J. Chem. Theory Comput.* **2015**, *11*, 132–138.
- (56) Kussmann, J.; Ochsenfeld, C. Preselective Screening for Linear-Scaling Exact Exchange-Gradient Calculations for Graphics Processing Units and General Strong-Scaling Massively Parallel Calculations. *J. Chem. Theory Comput.* **2015**, *11*, 918–922.
- (57) Kussmann, J.; Ochsenfeld, C. Pre-selective screening for matrix elements in linear-scaling exact exchange calculations. *J. Chem. Phys.* **2013**, *138*, 134114.
- (58) Bhattacharjee, A.; Andreiadis, E. S.; Chavarot-Kerlidou, M.; Fontecave, M.; Field, M. J.; Artero, V. A Computational Study of the Mechanism of Hydrogen Evolution by Cobalt(Diimine-Dioxime) Catalysts. *Chem. - Eur. J.* **2013**, *19*, 15166–15174.
- (59) Kaeffer, N.; Chavarot-Kerlidou, M.; Artero, V. Hydrogen Evolution Catalyzed by Cobalt Diimine–Dioxime Complexes. *Acc. Chem. Res.* **2015**, *48*, 1286–1295.

(60) Zhao, X.; Pachfule, P.; Li, S.; Langenhahn, T.; Ye, M.; Schlesiger, C.; Praetz, S.; Schmidt, J.; Thomas, A. Macro/Microporous Covalent Organic Frameworks for Efficient Electrocatalysis. *J. Am. Chem. Soc.* **2019**, *141*, 6623–6630.

(61) Zhao, X.; Pachfule, P.; Li, S.; Langenhahn, T.; Ye, M.; Tian, G.; Schmidt, J.; Thomas, A. Silica-Templated Covalent Organic Framework-Derived Fe–N-Doped Mesoporous Carbon as Oxygen Reduction Electrocatalyst. *Chem. Mater.* **2019**, *31*, 3274–3280.